Synthesis of layered silicon-graphene hetero-structures by wet jet milling for high capacity anodes in Li-ion batteries

To cite this article: Romeo Malik *et al* 2021 *2D Mater.* **8** 015012

2D Materials

OPEN ACCESS

RECEIVED
4 May 2020

REVISED
2 July 2020

ACCEPTED FOR PUBLICATION
14 July 2020

PUBLISHED
30 October 2020

PAPER

Synthesis of layered silicon-graphene hetero-structures by wet jet milling for high capacity anodes in Li-ion batteries

Romeo Malik[1], Qianye Huang[1], Laura Silvestri[2,3], Danqing Liu[1], Vittorio Pellegrini[3,4], Luigi Marasco[3], Eleonora Venezia[3], Sara Abouali[3], Francesco Bonaccorso[3,4], Michael J Lain[1], David Greenwood[1], Geoff West[1], Paul R Shearing[5] and Melanie J Loveridge[1]

[1] WMG, University of Warwick, Coventry, United Kingdom
[2] Dipartimento di Tecnologie Energetiche, ENEA C.R Casaccia, Roma, Italy
[3] Graphene Labs Istituto Italiano di Tecnologia, Genova, Italy
[4] Bedimensional Spa, Genova, Italy
[5] Department of Chemical Engineering, The Electrochemical Innovation Lab, University College London, London, United Kingdom

E-mail: M.Loveridge@warwick.ac.uk

Keywords: lithium-ion batteries, silicon, graphene, wet-jet milling, FIB-SEM tomography, high-energy-density electrodes

Supplementary material for this article is available online

Abstract

While silicon-based negative electrode materials have been extensively studied, to develop high capacity lithium-ion batteries (LIBs), implementing a large-scale production method that can be easily transferred to industry, has been a crucial challenge. Here, a scalable wet-jet milling method was developed to prepare a silicon-graphene hybrid material to be used as negative electrode in LIBs. This synthesized composite, when used as an anode in lithium cells, demonstrated high Li ion storage capacity, long cycling stability and high-rate capability. In particular, the electrode exhibited a reversible discharge capacity exceeding 1763 mAh g^{-1} after 450 cycles with a capacity retention of 98% and a coulombic efficiency of 99.85% (with a current density of 358 mA g^{-1}). This significantly supersedes the performance of a Si-dominant electrode structures. The capacity fade rate after 450 cycles was only 0.005% per cycle in the 0.05–1 V range. This superior electrochemical performance is ascribed to the highly layered, silicon-graphene porous structure, as investigated via focused ion beam in conjunction with scanning electron microscopy tomography. The hybrid electrode could retain 89% of its porosity (under a current density of 358 mA g^{-1}) after 200 cycles compared with only 35% in a Si-dominant electrode. Moreover, this morphology can not only accommodate the large volume strains from active silicon particles, but also maintains robust electrical connectivity. This confers faster transportation of electrons and ions with significant permeation of electrolyte within the electrode. Physicochemical characterisations were performed to further correlate the electrochemical performance with the microstructural dynamics. The excellent performance of the hybrid material along with the scalability of the synthesizing process is a step forward to realize high capacity/energy density LIBs for multiple device applications.

1. Introduction

Lithium-ion batteries (LIBs) remain the energy storage technology of choice for next-generation automotive and grid storage applications, to economically increase their energy/power densities and range longevity [1]. However, the dominant anode material in most commercially LIBs is still graphite, having a theoretical capacity limited to 372 mAh g^{-1} [2]. Silicon (Si) is foreseen as the contender for next generation anode materials owing to its high specific capacity (3579 mAh g^{-1}), availability, cost, and environmental benignity [3]. Recently, considerable studies have shown that crystalline silicon is a promising negative electrode candidate [4–6]. However, there is a need to re-design and modify Si-based anodes to overcome the physicochemical degradation of the electrode, resulting

from the electrochemically-driven volume expansion (>300%) from the lithium alloying reactions [4, 7]. Upon cycling, the continuous lithiation/delithiation of silicon can cause electrode pulverization, conductivity loss, continuous formation of unstable solid electrolyte interphase (SEI) film, determining capacity fade [8, 9]. Additionally, Si is a semiconductor, which prevents redox reactions and electron transport [10]. This electrochemical and mechanical instability of Si-based electrodes is currently precluding their commercial viability but remains a compelling research challenge [11].

To address the above issues, numerous approaches have been explored over the years to realise the potential of silicon anodes to achieve prolonged cycling. This includes reducing the particle size to nanoscale [12, 13], modifying the morphology of nanomaterials [14], distributing active silicon particles onto active/inactive host matrix [15], carbon lamination [16], binders systems [17, 18] and also by incorporating diverse additives-based electrolyte system [19, 20]. Researchers have found that one effective way to achieve prolonged cycling is to fabricate uniform distributions of active silicon nanoparticles (SiNPs) onto a flexible and conductive matrix, either to accommodate the volume changes in Si or to enhance electrical conductivity [21]. Recently, graphene-based materials have been exploited as a conductive additive in silicon-based anodes to substantially ameliorate concerns relating to Si as the dominant anode mass in LIBs [22–24]. Pristine graphene exhibits excellent electrical conductivity, mechanical strength and has a large surface area, providing substantial sites for Li^+ ion interaction- this makes it a preferential choice among other additives for silicon-based anodes [22, 25–28]. Furthermore, graphene's unique hierarchical structure and turbostratic distribution of the flakes when deposited as a coating, generates porous layers which enable the unrestricted flow of electrolyte throughout the electrode's architecture and operational lifetime [29]. The incorporation of graphene has been postulated to restrict electrochemical fusion of Si particles resulting from volume expansion upon lithium incorporation, whilst enhancing and maintaining the electrical contact between Si particles [30]. It maintains the electrode architecture against the huge volume changes from silicon and also improves the kinetics of the electrochemical reactions [30, 31]. A homogeneous distribution of active silicon particles within the matrix is crucial to achieve high performance LIBs. This is because SiNPs tend to agglomerate, which adversely affects the electrochemical performance [32]. Previous attempts to manufacture hybrid Si-graphene anode materials have been carried out by exploiting chemical vapour deposition [33, 34], atomic layer deposition [35], electrospinning [36], vacuum filtration [37–39], dip coating [40] and electrostatic spray deposition [41, 42]. However, these processes are complex and expensive. Also, in most cases, only thin coatings can be achieved, which are difficult to pair with high-energy density cathodes in order to manufacture full cells. In contrast to the aforementioned synthesis routes, here we demonstrate a high-pressure wet-jet milling method, previously developed to efficiently exfoliate graphite and produce few-layers pristine graphene flakes (FLG_{WJM}) [43]. Here, the graphite and Si particles are processed simultaneously leading to a Si-FLG_{WJM} composite that can be produced both in powder form or in solution and in large quantities (currently up to 1 kg per day in a lab-scale pilot line). This method does not require any pyrolysis steps and it is compatible with battery scale-up manufacturing lines, providing a facile and versatile approach to synthesize defect-free and high-quality multifaceted dispersion materials.

This novel strategy uses a liquid-phase mechanochemical approach in a continuous liquid flow, yielding a layer-by-layer structure. We found that the SiNPs are sandwiched in between the graphene flakes and interconnected in multiple directions with branch-like carbon black 'chains'. This interconnected porous framework is suggested to stably accommodate the volume expansion strains from SiNPs to facilitate and maintain transportation of electron and ions, in a mechanically robust microstructure. The evidence for this is based on studies of electrochemical impedance spectroscopy (EIS) combined with physical characterisation techniques able to image and quantify, over multiplescales, the evolution of internal morphology and the build-up of resistance [44].

To the best of our knowledge, the method here proposed yields the best capacity retention of any anodic materials proposed so far with such a large Si wt% content. To support this statement, table 1 outlines a range of other studies, which used a variety of methods to generate silicon-carbon composite materials. Some of these approaches used a considerably lower Si content than our study (50%–70%) and this is an important consideration when comparing electrochemical performance. We demonstrate a very large reversible gravimetric discharge capacity exceeding 1700 mAh g^{-1} (98% retention after 450 cycles with a coulombic efficiency of 99.85% with a current density of 356 mA g^{-1}). This combined with the industrial compatibility of the composite production process, make these findings of significant interest for further testing within an industrial environment.

2. Results and discussion

The Silicon-graphene hybrid material directly obtained through a wet jet milling process

Table 1. Summary of cyclability performance of Si-carbon electrode through different approaches.

Silicon	Carbon	Si wt%	Synthesis method	Current density (mA g^{-1})	Voltage range (V)	CE 1st cycle	Capacity retention	Capacity (mAh g^{-1})	Ref.
Ant-nest-like microscale porous Si	5–8 nm thick carbon layer	/	Thermal nitridation of the Mg-Si alloy in nitrogen (N_2)	2100	0.01–1	80.3%	90% after 1000 cycles	1271@1000 cycles	[45]
Silicon nano-particles	Carbon black	50	Si CVD deposition onto the annealed carbon black	3670	0–1.1	>85%	/	≈1600@100 cycles	[46]
Amorphous Si	Hollow carbon nano-spheres/Al2O3	62.5	PECVD	1000	0.01–1	81%	85% after 100 cycles	1560@100 cycles	[47]
Micron-sized Si	B4 C/graphite	40	Ball Milling	1260	0–1.5	82%	94% after 100 cycles	822@100 cycles	[48]
Si-nanolayer	Graphite/Carbon	9	CVD	358	0.005–1	92%	96% after 100 cycles	517	[49]
Si nanoparticles	Graphite	20	Carbonization	130	0.01–2	80%	82% after 50 cycles	712@100 cycles	[50]
Si nanoparticles	Graphene oxide	46	Sol-gel method + carbonization	100	0.02–1.5	56.6%	83% after 100 cycles	700@100 cycles	[51]
Si nanoparticles	Carbon layer	12.5	Spray drying + CVD	358	0.005–1	89%	80% after 250 cycles	≈600@100 cycles	[52]
SiO	MgO/graphite	25	Ball Milling	/	0.01–1.5	77%	90.7% after 74 cycles	630@75 cycles	[53]
Si nano-powder	Graphite oxide	45–55	filtration method	50	0.02–1.2	58%	/	708@100 cycles	[39]
Silicon nano-particles	Graphite oxide	50	filtration method	50	0.05–1.5	63%	94% after 30 cycles	786@300 cycles	[54]
Silicon nano-particles	Graphene oxide	46	Self-assembly	500	0.001–2.5	/	83.4 after 50 cycles	1481@50 cycles	[55]
Si nanoparticles	Few-layer graphene sheet	50	Wet Jet Milling	358	0.05–1	84%	98% after 450 cycles	1763@450 cycles	Our work

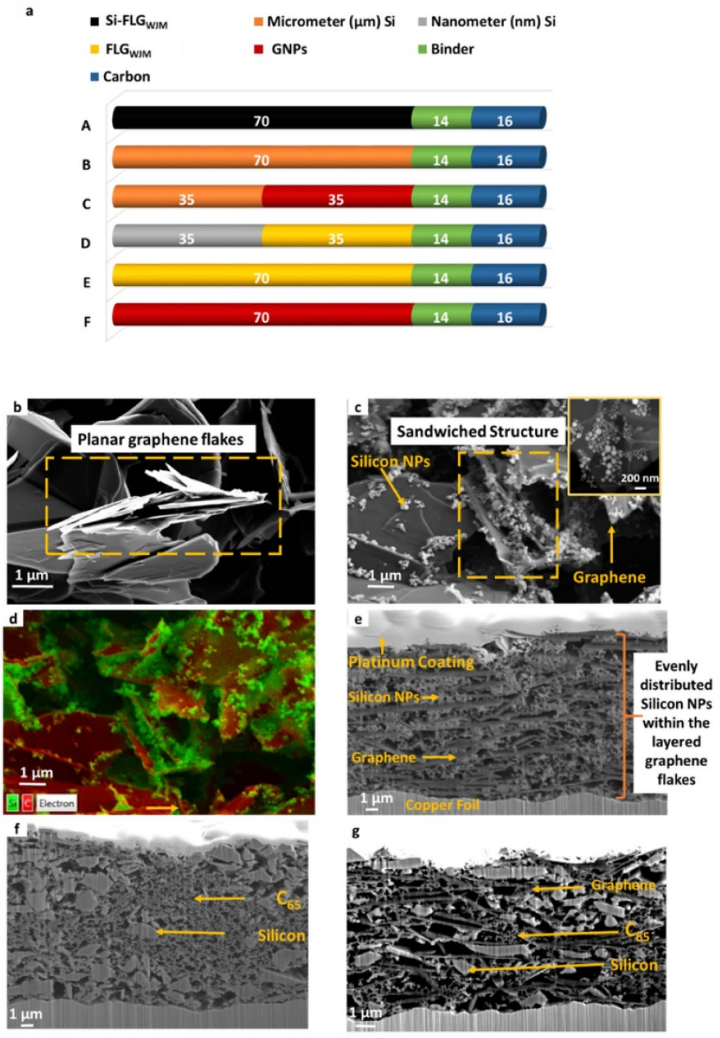

Figure 1. (a) Schematic formulation matrix; SEM images of (b) FLG$_{WJM}$ powder, (c) as-synthesised Si-FLG$_{WJM}$ (zoomed Si-FLG$_{WJM}$ powder as inset) with (d) energy dispersive spectra (EDS) derived chemical distribution maps showing the presence of Si in the planar flakes of FLG$_{WJM}$; cross-section images of electrode with (e) Formulation A—Si-FLG$_{WJM}$ composite, (f) Formulation B—Si-dominant, and (g) Formulation D—composite nm Si with FLG$_{WJM}$ powder.

(Si-FLG$_{WJM}$) was used to prepare electrodes for electrochemical characterization by the addition of a conductive carbon(Super C65, TIMCAL C-NERGY) and a polymeric binder, *i.e.* PAA-Na, with a weight ratio of active material: polymeric binder: conductive carbon of 70:14:16. Figure 1(a) shows a scheme of the sample formulations reported and tested in this study. Formulation A indicates the electrodes based on Si-FLG$_{WJM}$ material. Furthermore, to compare the influence of Si particles dimension, graphene type and hybridisation approach, five additional electrode formulations were used. Basically, Si-FLG$_{WJM}$ performance in lithium cells have been compared to: (i) a Si-dominant electrode prepared with micrometric silicon (μmSi) particles and labelled as Formulation B; (ii) a composite prepared using μmSi particles and commercial graphene nanoplatelets (GNP, consisting of flakes with lateral dimensions of a few microns and thickness of 6–8 nm) and labelled as Formulation C; (iii) a composite obtained by the mixing of SiNPs and FLG$_{WJM}$ (Formulation D); (iv) FLG$_{WJM}$ based electrode as Formulation E and, finally, (v) GNP based electrode labelled as Formulation F. For all the Si-graphene composites, the weight ratio has been kept 1:1.

2.1. Structure and morphology

Ample sharp folds or defects on the FLG$_{WJM}$ flakes may act as anchoring region for SiNPs. Figures 1(b)–(g) shows the SEM images of the pristine powders (on the top) and the electrodes cross section (below). The FLG$_{WJM}$ powder synthesized via mechanochemical wet-jet milling exhibits a parallel planar morphology of large FLG$_{WJM}$ flakes (figure 1(b)). The detailed characterization of FLG$_{WJM}$ is reported by Del Rio Castillo *et al* [43]. In the Si-FLG$_{WJM}$ composite (figures 1(c) and (d)) we can observe that SiNPs, having a dimension of *c.a.* 100 nm in diameter, are homogeneously distributed on the surface of the FLG$_{WJM}$ flakes and anchored on and between the FLG$_{WJM}$ flakes stacks.

Looking at the electrode cross section (figure 1(e)), in the electrode with Si-FLG_{WJM} (Formulation A), it is interesting to note that FLG_{WJM} encompasses the SiNPs forming a sandwich-like 3D structure. Such structural arrangement is not visible in the other two formulations, in which the two components were simply co-dispersed and not processed by wet jet milling (figures 1(f), (g) and S1(a) (available online at stacks.iop.org/2DM/8/015012/mmedia)).

Furthermore, it is evident that the retention of SiNPs onto FLG_{WJM}'s surface is maintained, despite undergoing high shear mixing during electrode dispersion preparation. This demonstrates a good degree of Si-FLG_{WJM} powder's structural integrity and robustness. It can be seen in the cross-sectional image of figure 1(e), that the FLG_{WJM} flakes form a continuous conductive network throughout the Si particles, and to the current collector, resulting in a mechanically robust sandwich-like architecture. This inter-connected layered arrangement may promote a higher rate performance and prolonged cycle life [40], further supported later in this report by an impedance study and supported by previous literature [27, 28, 56–58]. From the above microstructural analysis, it can be concluded that the Si-FLG_{WJM} composite (figure 1(e)) via wet-jet milling approach containing SiNPs is well distributed throughout the FLG_{WJM} matrix. The homogenous spread of porosity is visible in the layered composite. We conclude by pointing out that the exploited synthesis route is economical and scalable compared to the majority of the chemical methods.

2.2. Electrochemical characterisation

The electrochemical performance of the Formulation A electrode was verified in lithium cells by galvanostatic cycling in the voltage range of 0.05–1 V at 0.2 C (1 C = 3579 mA g^{-1}) and compared it with the other five formulations described in figure 1(a). When cycling at the full capacity of Si (corresponding to a current density of 716 mA g^{-1} at 0.2 C) we expected to verify the contribution of graphene on the structural integrity and capacity retention, given its favourable tensile properties. Furthermore, to minimize the volume expansion and thus avoid the likelihood of pulverization, the cells were cycled also using a limited charge (lithiation) capacity of Si, *i.e.* 1800 mAh g^{-1} [59].

Figures 2(a) and (b) show the cycling behaviour in lithium cell of the Formulations A–D under galvanostatic cycling conditions (specific capacity is referred to the mass of silicon in the electrode). When cycled without any capacity limitation, as reported in figure 2(a), we observe a continuous capacity decrease as a function of cycle number, for all the cells, particularly evident during the first 20 cycles. All formulations are able to achieve a discharge specific capacity of ≈3000 mAh g^{-1} at the end of first cycle. However, Formulation A (green curve in figure 2(a)) demonstrates to maintain higher capacity values during prolonged cycles and, after 50 cycles, the capacity seems to stabilize at around 2300 mA g^{-1}. Looking at the other formulations, particularly evident are the differences between the Formulations A and D (both prepared starting from nm Si and FLG_{WJM}) and Formulations B and C (prepared using μm Si and/or GNPs). Formulation D, similarly to Formulation A, exhibits a more stable cycling profile. However, the discharged specific capacity achieved after 50 cycles is lower in comparison to Formulation A (2000 mA g^{-1}, 13% lower than Formulation A). This observation further confirms the effectiveness of using wet-jet milling approach for simultaneous exfoliation of graphite and uniform dispersion of nmSi in between the FLG_{WJM} layers. The shear force applied during the wet-jet milling process, results in better distribution of nm Si in the matrix. During the subsequent charge/discharge cycles, there is less possibility for the re-agglomeration of nm Si and consequently, a lesser degree capacity fading is observed in the initial cycles. It is evident that in both Formulations C and B present a discharge capacity that decreases more rapidly. In particular, Formulation B, consisting of μm Si without graphene, achieves half of the initial specific capacity only after 100 cycles.

Compared with Formulation B, the addition of GNPs (Formulation C) is able to improve the performance of this type of silicon. In summary, Formulation A, the composite prepared by wet jet milling, shows higher discharged capacity values compared with all the other formulations. It is worth mentioning that electrodes with more Si-FLG_{WJM} powder and less additive mass (Si-FLG_{WJM}/carbon/binder: 90/5/5) were also prepared. The cyclic performance is compared with the electrodes with more additives in figure S2. Whilst the trend is similar for both formulations after 80 cycles, the specific capacity is lower for the electrode with reduced additive mass, which can be attributed to in part by the lower conductivity of the electrode. Additionally, a lower amount of polymer binder will influence the cohesive and adhesive connections to the current collector, which will relate to resistance changes.

The electrochemical behaviour observed for Formulations B and C is likely to be related to the larger Si-particle dimensions, resulting in pulverisation and higher tortuosity for Li-ion transport. As a consequence, an increase in the cell resistance is expected, while it seems that this phenomenon is alleviated in the case of nm Si particles, as the ones used in Formulations A and D.

The electrochemical performance of the cells showed in figure S3 has been reported calculating the specific capacity related to the whole mass of electrode (active material, conductive carbon and binder) and related to the mass of active materials, including

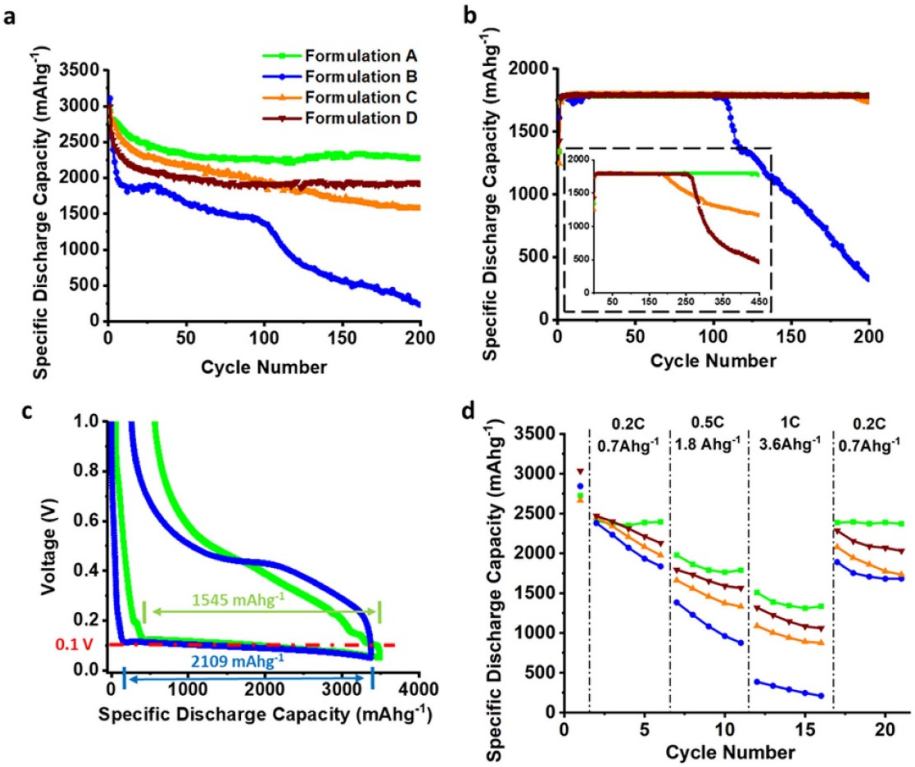

Figure 2. Specific discharge capacity or de-lithiation (based on the silicon's active mass) profiles of formulations cycled at (a) full capacity of silicon (3579 mAh g^{-1}), (b) half capacity of silicon (longer cycling of all Si-FLG hybrid electrodes are shown in the inset), (c) first lithiation-delithiation voltage profiles for Formulation A and B, and (d) rate capability test for all the formulations. The legends for (a) also apply to (a)–(d). For all the electrochemical tests, a first cycle at C/20 has been applied as the formation cycle.

as active material also the graphene for the composite electrodes. The results are reported in figure S3. As observed in figure S3(a), Formulation A at the end of the first cycle achieves a specific capacity of almost 1500 mAh g^{-1} (referred to the mass of Si + graphene) that decreases to 1200 mAh g^{-1} after 50 cycles (at 0.2 C). Despite the capacity values becoming reduced compared with the data reported in figure 2(a), this electrode is still able to exibit high reversible capacity values. Also in this case, Formulation A was compared with the other Formulation B–D, as showed in figure S3(b). This comparison further confirms that Si-FLG_{WJM} electrode prepared by the wet jet milling procedure offers better electrochemical performance in terms of reversible specific capacity and cyclability. To better appreciate the results obtained, we also calculated the "theoretical" specific capacity related to the total mass of Si-FLG_{WJM} electrode based on the performance in lithium cell of graphene dominant electrodes (Formulations E-F) as reported in figure S4. For Formulation A, the maximum capacity value obtained during cycling, the specific capacity associated with the total mass of silicon and graphene is 54.6% and 45.4% respectively. This is according to TGA measurements, figure S10. Considering Formulation A, based on the specific capacity obtained during the first lithiation at C/20, *i.e.* 3372 mAh g^{-1} for Si and 300.7 mAh g^{-1} for FLG_{WJM}, the "theoretical" specific capacity can be calculated as 1977 mAh g^{-1}. The analysis confirms that Formulation A shows a very promising electrochemical performance, reaching a value very similar to the considered "theoretical" capacity. However, from figure S4, we have to note that the graphene dominant electrodes present a large irreversible capacity with a large first cycle loss of 80.21 mAh g^{-1} and 251.77 mAh g^{-1}, for FLG_{WJM} and GNPs, respectively. In fact, when cycled at 0.2 C after the first formation cycle, the FLG_{WJM} can contribute only around 143.27 mAh g^{-1}, whilst GNPs contribute to 127.40 mAh g^{-1} reversibly after 200 cycles. The reversible capacity obtained from the graphene-dominant electrodes was lower than reported in a previous study [31] and this is due to the higher applied current density (*i.e.* 715.8 mA g^{-1} in comparison to the literature's 357.9 mA g^{-1}) in this study.

Further improvements in the electrochemical performance are obtained by cycling the cell at limited capacities (50% of capacity, *i.e.* 1800 mAh g^{-1}) as shown in figure 2(b). It should be noted that all the graphene-containing formulations cycled up to 200 cycles with a current density of 358 mA g^{-1}.

Formulation A has shown prolonged cycle life with almost no capacity degradation even after 450 cycles (figure 2(b)), compared with other formulations comprising graphene, *i.e.* GNPs, (Formulation

C and D). The main reason for capacity loss in Formulation C and D is most likely attributed to the collapse of the electrode's architecture (microstructure) with continuous growth of SEI (common with Si materials). This further results in the pore clogging and increased resistance towards Li^+ ion movement [44, 60, 61], as discussed in the following sections (where we present the tomography and impedance studies). From the cycling profiles, it is evident that the incorporation of graphene in the Si-electrode has a significant and positive effect on the cyclic stability, and that the Si-FLG_{WJM} composite produced by the mechano-chemical method via continuous liquid exfoliation provides the superior performing materials.

The lithium intercalation behaviours of commercial GNPs and FLG_{WJM} are similar to that of microcrystalline graphite [30]. However, studies have shown that with decreasing flake thickness additional strain is exerted upon the graphene flakes during ion insertion [62]. The voltage profiles (voltage vs. capacity) for the first cycle of the hybrid Si-FLG_{WJM} powder composite and Si-dominant electrode is shown in figure 2(c). With the incorporation of graphene into the system, the lithiation capacity below the characteristic 0.1 V had decreased by 27% in comparison to the Si-dominant electrode. This can be attributed to the electrochemically activity of FLG_{WJM} which participates in the lithiation process between 0.9–0.1 V, but to a much lower lithiation capacity.

During the first lithiation step, below 0.1 V, the two samples show a similar behaviour: a long flat plateau characteristic of silicon anodes (vs Li) and corresponding to the formation of amorphous metastable lithium silicide phase (a-Li_xSi) via solid-state amorphisation [63, 64]. Conversely, during the de-lithiation step, the two voltage profiles are quite different. The addition of graphene in the composite leads to a reduction of discharge/charge hysteresis loop. Furthermore, at lower potential (around 0.1 V) it is possible to detect two little plateaus, related to the contribution of graphene in the redox process.

We further explored the rate performance of all the formulations at different current densities including, 0.2 C, 0.5 C, and 1 C (figure 2(d)). As can be seen from figure 2(d), the first cycle at C/20 shows some differences with the cycling behaviour reported in figure 2(a). Nevertheless, the capacity values can be considered comparable, since for all cells they remain higher than 2800 mA g^{-1}.

Focusing on the electrochemical performance, the Si-FLG_{WJM} composite electrode possesses 81.77% of its initial capacity at 0.2 C. By increasing the current density, the reversible capacity drops to 1789.08 mAh g^{-1} at 0.5 C (61.13% retention) and subsequently to 1333.09 mAh g^{-1} at 1 C (45.55% retention). Upon lowering the current density to 0.2 C, the reversible capacity of Si-FLG_{WJM} composite increases to 2371.27 mAh g^{-1} at 0.2 C (81.03% retention). Thus, Si-FLG_{WJM} composite electrode is presumed to undergo a minimal degradation under higher current density. This is due to the conductive network and buffering of the volumetric changes exerted from SiNPs.

In order to augment our understanding of the hybrid composites, the redox reactions and the transformation steps of Si-FLG_{WJM} composite vs Li/Li^+ during lithiation/de-lithiation processes were analysed. The differential capacity plot (dQ/dV vs. V) in figure 3(a) shows more details on the electrochemical reactions taking place during lithiation and de-lithiation vs. Li/Li^+. Upon lithiation, the Si-dominant electrode shows two redox peaks corresponding to the formation of the amorphous $Li_{3.5}Si$ [30, 64–67]. In contrast, in the Si-FLG_{WJM} composite electrode we can observe the appearance of three additional peaks corresponding to the contribution of FLG_{WJM} in the redox process. Herein, during lithiation, the fourth cathodic peak encompasses two reactions corresponding to the formation of LiC_{12}. Furthermore, the cathodic peak at 0.06 V is attributed to the formation of LiC_6 [64]. Similar to the lithiation process, five stages can be detected during the de-lithiation process in the Si-FLG_{WJM} composite electrode, corresponding to the reformation of a-Si and LiC_{72} [30, 66].

It can also be seen that with increasing cycle number there is a decrease in peak intensity and also a shift in the redox peak voltages (see figures 3(b) and (c)). The above can be attributed to the increase overpotential within the electrode *i.e.* impedance increases due to a continuum of SEI growth and architectural breakdown. In particular, after 200 cycles, the areas beneath the lithiation peaks have decreased by a significant amount for the Si-dominant electrode compared with the Si-FLG_{WJM} composite electrode. In conclusion, as expected, the differential capacity plot of the Si-FLG_{WJM} composite indicates that both Si and FLG_{WJM} are electrochemically active within the operating potential range.

Figure 3(d) displays comprehensive data on the first cycle and after 200 cycles. For Si-FLG_{WJM} composite (Formulation A), the first cycle coulombic efficiency is 84%, slightly lower than for the Si-dominant system (Formulation B). The lower first cycle coulombic efficiency in the composite (Formulation A) can be accredited to a greater electrolyte decomposition on the large surface area of FLG_{WJM} and SiNPs. Nevertheless, from figure 3(d) it is worth noting that all the Si-FLG hybrid formulations are very promising anodes for their highly stable reversible capacity cycling in comparison to the Si-dominant electrode. The Si-FLG_{WJM} electrode (Formulation A) offers a reversible discharge capacity of 2280.71 mAh g^{-1} with capacity retention of 77.81% after 200 cycles with a capacity loss of only 0.11% per cycle, a value that is superior to previously reported Si-graphene-based hybrid anodes in the literature [21, 55, 58, 68–70].

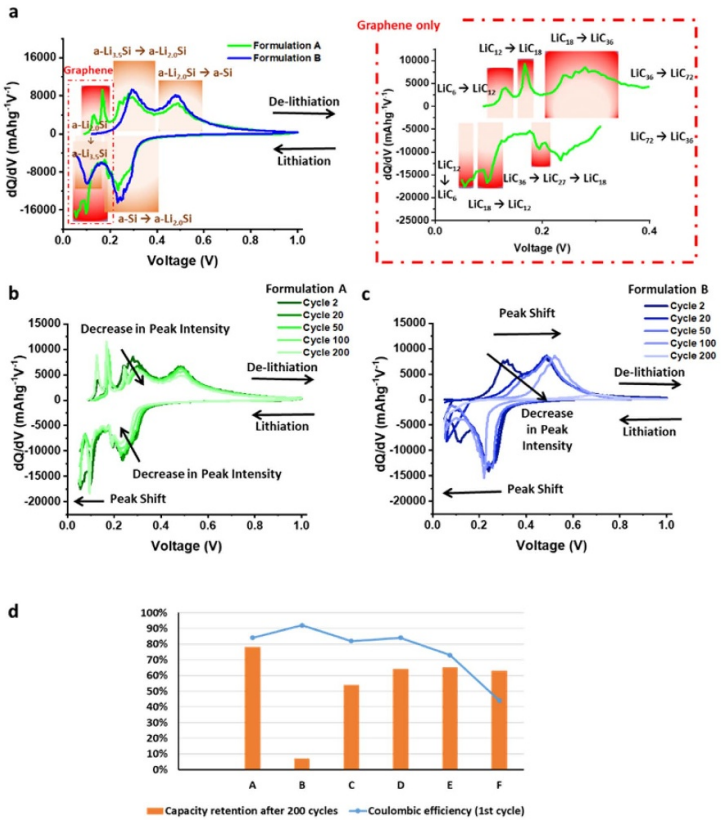

Figure 3. (a) dQ/dV plot for 2nd cycle of Si-FLG$_{WJM}$ composite electrode (Formulation A) and Si-dominant electrode (Formulation B) relatively (dQ/dV profile for FLG$_{WJM}$ (Formulation A) between 0.0–0.4 V is shown as the inset); dQ/dV plot with incremental cycle numbers for (b) Formulation A and (c) Formulation B; (d) Formulation comparison of capacity retention (after 200 cycles) and first cycle coulombic efficiency (%). Presented data are for the cells cycled at full capacity of silicon.

The beneficial effect of the commercial GNPs for the electrochemical performance of silicon can be noticed also in Formulation C composite that exhibits enhanced cycling performance compared with the Si-dominant formulation (Formulation B), which exhibits 87% less specific capacity. However, when compared to the other formulations (Formulation B, C and D), the Si-FLG$_{WJM}$ composite by wet jet milling (Formulation A) displays improved capacity retention. The coulombic efficiency for all the formulations are shown in figure S5.

In summary, the reversible capacity retention of Si-FLG hybrid systems are consistently higher than the Si-dominant electrode for all the different current densities tested. Both the cycling stability and rate capability confirm that the Si-FLG$_{WJM}$ composite (Formulation A) is more resilient to capacity fade from volume expansion strain in comparison to other graphene incorporated Si anodes. Alongside the unique morphology of Formulation A, the 3D porous layered structure of the electrode attributes to the superior cyclability. Herein, the poor capacity retention in Si-dominant electrodes is attributed to the higher resistance from continuous growth and breakdown of SEI along with a diminishing pore network. Therefore, the Si-FLG$_{WJM}$ composite electrode displayed superior cyclic performance, which could be ascribed to the unique porous multilayered morphology of the electrode. The FLG$_{WJM}$ flakes provide structural rigidity and hinders Si particles from detaching due to pulverization, from the FLG$_{WJM}$ matrix. Finally, it is conceivable that the stability of Formulation C underwent structural degradation under higher current density due to larger Si particle size in comparison to the ones used in Formulation A.

2.3. Morphology evolution

In order to directly correlate the electrode microstructure to the batteries performance, we exploited focused ion beam in conjunction with scanning electron microscopy (FIB-SEM) tomography to study 3D microstructure of battery materials (see figures 4(a) and (b)) [71–74].

FIB-SEM tomography provides high resolution, down to tens of nanometers, which is otherwise below the capability limits of the conventional laboratory source X-ray technique [75]. FIB-SEM tomography not only enables visualisation but also quantitative evaluation of the complex geometrical parameters like phase volume fractions, phase surface areas, electrode thickness, phase size distribution, and porosity [76–83]. The high resolution allows for a detailed study of finer pore sizes and different

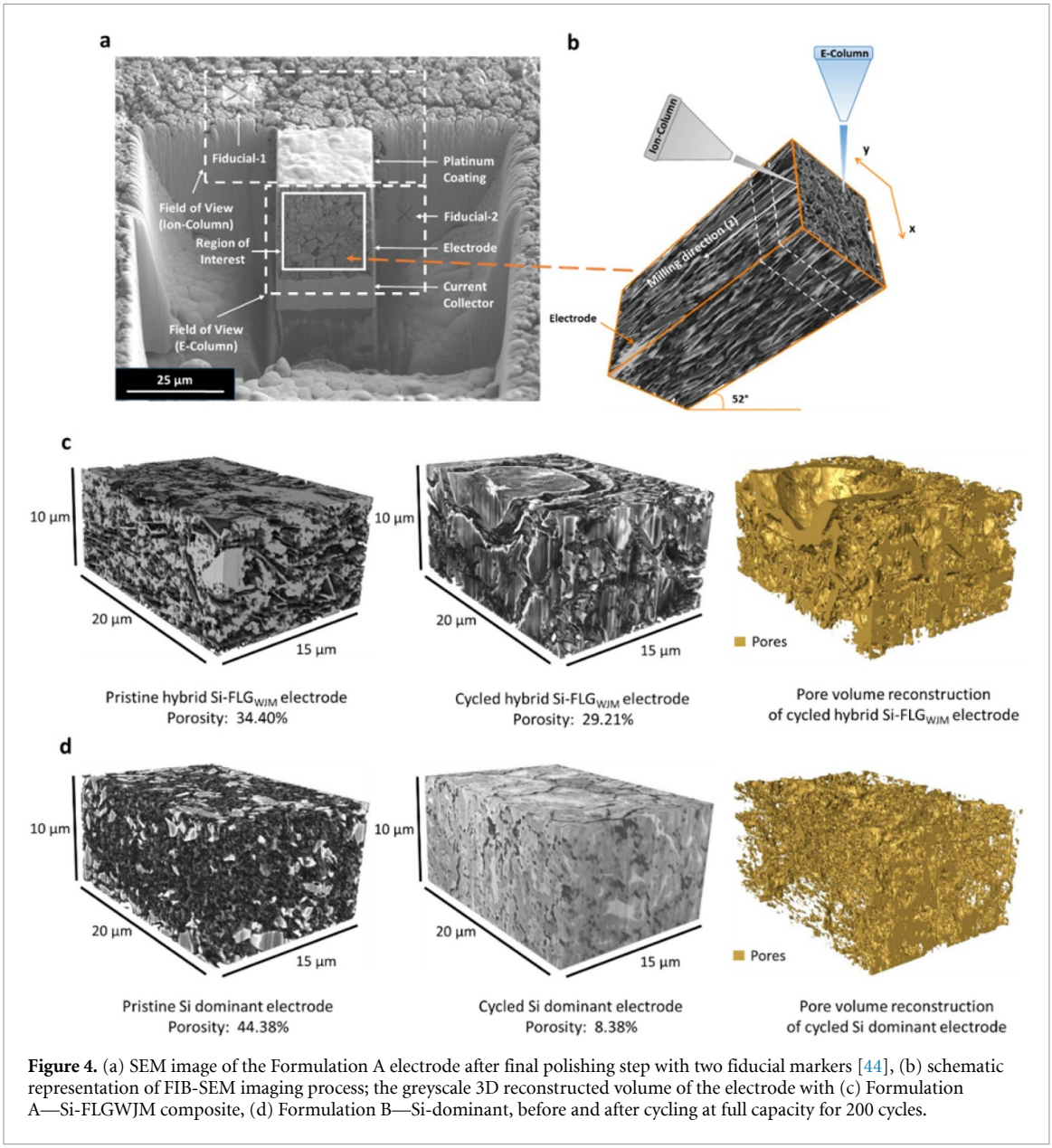

Figure 4. (a) SEM image of the Formulation A electrode after final polishing step with two fiducial markers [44], (b) schematic representation of FIB-SEM imaging process; the greyscale 3D reconstructed volume of the electrode with (c) Formulation A—Si-FLGWJM composite, (d) Formulation B—Si-dominant, before and after cycling at full capacity for 200 cycles.

phases involved. This provides insights in clarifying structure-property-performance relationships.

Porosity plays a key role in cell performance through the electrochemical reaction kinetics, as well as the Li^+ ion's transport properties including tortuosity [44, 84]. The morphological evolution of the Si-FLG$_{WJM}$ composite (Formulation A) and Si-dominant (Formulation B) for pristine electrodes and cycled electrodes (200 cycles) were analysed using (FIB-SEM), which allows for the visualization and quantification at the three-dimensional (3D) scale [74, 82, 83, 85, 86]. The morphological evolution for remainder formulations are shown in figures S6, S7 and S8. These studies are precious to offer more evidence of the benefits on the electrode structural changes brought by the incorporation of graphene in silicon-based anodes. Results are given in figures 4(c) and (d) that reports the comparison of Si-FLG$_{WJM}$ composite electrode (Formulation A) and Si-dominant (Formulation B) before and after cycling. The region of interest for our samples ranged between 25 × 10 μm^2 to 25 × 33 μm^2, since the cycled electrodes had a variable change in thickness. From this, we obtained a 3D reconstructed volume of 20 × 10 × 15 μm^3 across all the samples. The porosity can be calculated from the processed images. Figures 4(c) and (d) highlight a segregation of pore groups upon cyclic aging. In Si-dominant electrodes (Formulation B), merging among the particles in the cycled electrodes can also be seen. This is most likely to result from the huge volume expansion and electrochemical fusion of particles—similar to observations made in previous studies [32, 44, 87]. Despite the coalescence of SiNPs after cycling, cycled Si-FLG$_{WJM}$ electrodes were found to retain their porous 3D morphology (figure 4(c)). The 3D conductive network from FLG$_{WJM}$, along with the flexibility from the nano-flakes, plays favourable towards the electrode's

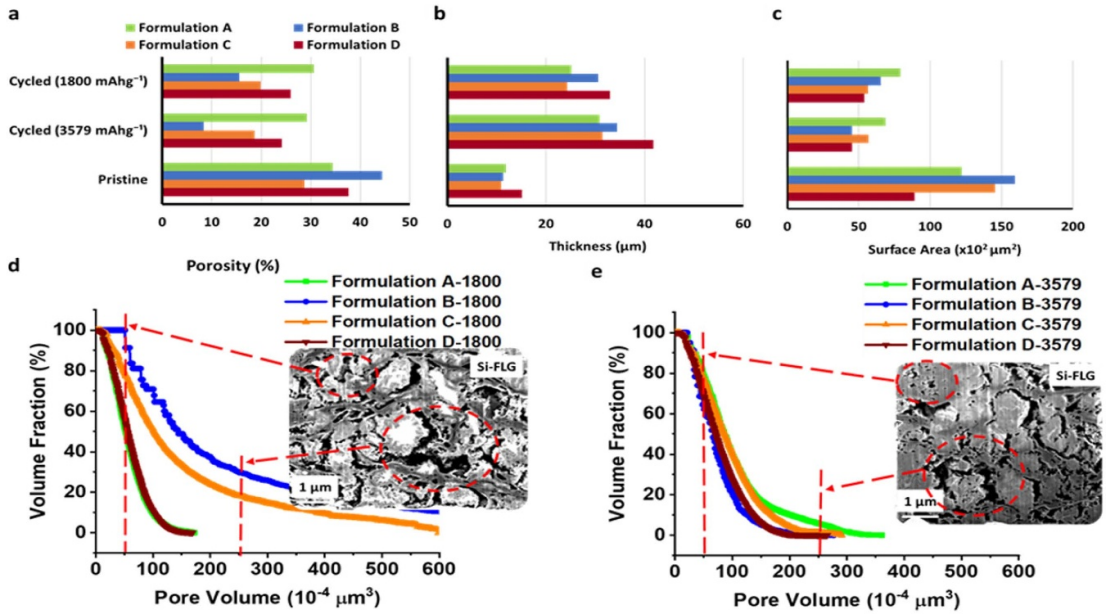

Figure 5. Geometrical property comparison after cycling at silicon's half and full capacity. Electrode's (a) porosity, (b) thickness and (c) pore surface area comparison; cumulative pore volume distribution comparison of all cycled electrodes with (d) half capacity of silicon, (e) full capacity of silicon (the insets show cross-sectional SEM images for Formulation A after 200 cycles under half and full capacity, respectively). The legends for (a) also applies to (b), (c).

stability during lithiation/de-lithiation. This accommodates the huge volume changes of SiNPs while maintaining electrical connectivity of all throughout the electrode.

The fact that Si-FLG$_{WJM}$ hybrid electrodes shows superior additive properties in comparison to Si-dominant electrode could be attributed to an increased innate structural flexibility of the coating [35]. As shown in figure 5(a), the porosity retention (after 200 cycles) is higher in all Si-graphene-based hybrid anodes (Formulation A, C and D) in comparison to the Si-dominant electrode (Formulation B). When SiNPs are used, it can be seen that the porosity of the cycled electrodes at full capacity decreases by only 15% and 36% for the Formulation A and D, respectively (see figure 5(a)). This implies again the benefit of using wet-jet milling process to uniformly disperse nmSi in the graphene matrix compared to a simple dispersing method in Formulation D.

In particular, with cells cycled at half capacity, it can be seen that the Si-FLG$_{WJM}$ composite (Formulation A) shows little change in porosity of ~11% compared to the pristine electrode. In this sense, these pores also help to maintain sufficient void structure around the active particles proving 'ion-conducting channels' to the electrode architecture [44]. Reduced porosity or increased tortuosity may adversely affect the lithium permeability and diffusion into the active material, resulting in capacity loss [44]. The observation of cracks on the electrode surface is consistent with previously reported studies [32, 44, 88, 89]. This observation can also be supported by the tortuosity factor and impedance studies for the electrodes, which will be extensively discussed in the following sections.

The presence of graphene in the electrode believed to buffer the stresses in the structure during lithiation of Si, and this influence is very much evident in the electrode's thickness post-cycling. The initial thicknesses of the pristine electrodes were recorded as well as the post-cycling thicknesses (see SEM and FIB-SEM characterisation methods for details) and they are shown in figure 5(b). In the case of electrode with µm silicon particles (Formulation B) there is an increase in the thickness of electrodes after cycling at full capacity by >204%. Whilst the thickness value post-cycling decreases to 160%, 176% and 187% in the Si-FLG$_{WJM}$ composite (Formulation A), nm Si with FLG$_{WJM}$ (Formulation D) and µm Si with the commercial GNPs (Formulation C), respectively (see figure 5(b)).

Another observation is that electrodes containing graphene that have been cycled at half capacity, have a lower increment in the electrode thickness with respect to Si-dominant electrodes cycled at full capacity of silicon. Comparing the surface areas in contact with the electrolyte for a pristine electrode and a cycled electrode, as reported in figure 5(c), it can be seen that there is a large decrease in the specific surface area for all the formulation. Specifically, in the Si-dominant electrode (Formulation B) the surface area is reduced of >61%. This value slightly decreases when the commercial GNPs is added (Formulation C). In contrast, for the Si-FLG$_{WJM}$ composite (Formulation A) and nm Si with FLG$_{WJM}$ (Formulation D) is ca. 43% and 49%, at full capacity,

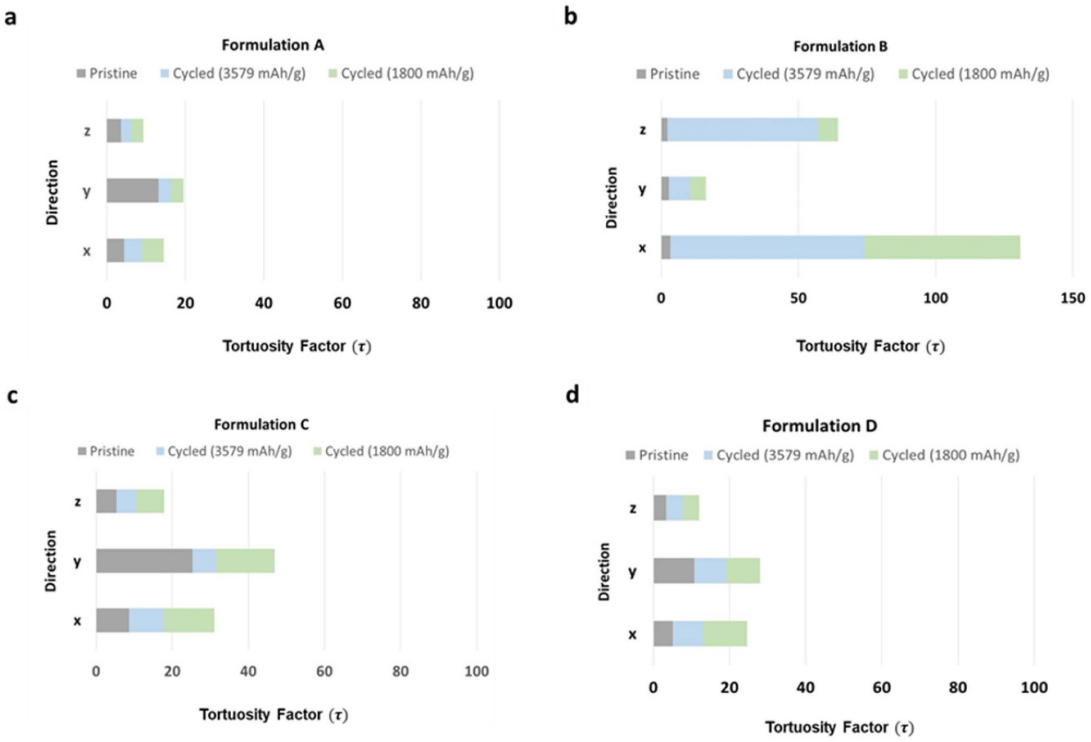

Figure 6. Tortuosity factor comparison between pristine electrodes and cycled electrodes after 200 cycles at Si's half and full capacity cycling for Formulations: (a) A; (b) B; (c) C and (d) D.

respectively (see figure 5(c)). All formulations are seen to have reduced surface area and porosity upon full lithiation, with a parallel increase in electrode thickness.

We also calculated the porous volumes of the electrodes after cycling. As observed in figures 5(d) and (e), there is a significant change in the pore volume after 200 cycles for each of the electrode formulations. Upon aging, there is a shift towards the lower end of the pore volume spectrum, which may be an indication that the pore volume becomes reduced due the electrochemical fusion of the expanded Si particles in Si-dominant anodes (Formulation B). However, upon careful observation in figures 5(d) and (e) it can be seen that there are many pores with large volume, which can be explained by the large volume expansion and pulverisation that active silicon particles undergo [44]. This is believed to correlate with a decrease in charge transfer impedance upon full capacity cycling [44], and will be discussed later on in section 2.5.

The FLG_{WJM} component in Formulation A electrodes facilitates a flexible-porous network for the active silicon particle undergoing volume changes upon lithiation and de-lithiation and maintaining 'ion-conducting channels' for the electrolyte. Overall, results in figure 5 offer direct evidence of Si-FLG_{WJM} composite as the superior structure bestowing larger pore channels, longer and flexible conductive network, to tolerate the continuous volumetric strains from silicon particles upon cycling. Therefore, it can be concluded that by accommodating volume expansion, the electrode structure is more robust and experience less electrochemical fusion. For cells cycled under full capacity, this particle fusion (incorporating SEI) is more significant with continual SEI growth and particle cracking dominating cell degradation. Further, the thickness and surface area change for graphene dominant formulations are presented in Table S1 and S2. The graphene-dominant electrode's analysis shows that the FLG_{WJM} is much more electrochemically stable and robust compared to the commercial GNPs.

2.4. Tortuosity factor calculation

The tortuosity factor (τ) is an important parameter which is directly proportional to the ionic transport property of ions through pores [44, 90]. τ is calculated by simulating the steady-state diffusion flow through the 3D pore network [44, 91]. In our work, tortuosity is calculated using the reconstituted structures from FIB-SEM characterisation, and figure 6 presents a series of measurements comparing pristine electrodes with those of cycled electrodes at full and half capacities. Formulations A to D were analysed in three directions x,y,z in the electrode areas sampled. Formulation A (figure 6(a)) has clearly retained the lowest τ values in all directions in both the pristine and post 200 cycled samples. This is in alignment with the resulting superior electrochemical performance of the Si-FLG_{WJM} electrodes in terms of a retained

higher level of cycling efficiency and longevity. Formulation D (figure 6(d)) also maintains a comparable level of x-y-z tortuosity after 200 cycles; these were based on a composite electrode of nano Si powder and FLG_{WJM}. Formulation B (figure 6(b)) demonstrated the highest level of tortuosity (especially in the x direction). These electrodes, based on predominantly micron-Si, experience the highest degree of volume expansion and particle fusion. This will dominate the structural transformation and it is consistent with the porosity reductions outlined in figure 5. Tortuosity values calculated for Formulation C (figure 6(c)) were between those of A and D and of B; these electrodes were based on a composite of FLG_{WJM} and micron-Si. The FLG_{WJM} enables porosity retention, mechanical resilience and also reduces the degree of electrochemical fusion of micron-Si particles. Long-range electrical conductivity also improves charge transfer levels—this is discussed in more depth in the next section on impedance characterisation. From figure 6 generally, it can be seen that τ values for each of the electrodes decrease upon cycling at full capacity, except for the formulation Si-dominant (Formulation B). The explanation for this is that the Formulation B does not have any flexibility effect, which can help to sustain the volume changes, thereby the mesopores are continually filled by fragmented SEI layers.

For electrodes cycled at full capacity, τ decreases, as the volume changes from silicon particles have resulted in macro-voids and these cracks act as carrier path for the electrolyte [44]. The gradual decline of pore volume with broken SEI impedes the flow of Li^+ ions through the porous network [44]. The architectural fragmentation is minimal in the Si-graphene hybrid anodes as inferred from impedance measurements reported in the following section and also reflected inτ.

Formulations with Si-FLG_{WJM} (Formulations A and D), when cycled at full capacity, have a lower τ when compared with cells cycled at half capacity [44]. At full capacity, the electrode undergoes macro cracking with large volume changes exerted from the silicon fraction. It is assumed that Si's electrochemical fusion has been prevented by incorporation of graphene.

2.5. Electrochemical impedance spectroscopy studies

The significance of incorporating graphene to improve the electrodes structural stability is further demonstrated by the sizeable improvement in the impedance relative to that of the Si-dominant anode. Measurements were taken every 10 cycles. The equivalent circuit used for the calculations is shown in figure 7(a).

In Nyquist plots showed in figures 7(b)–(d) and (h)–(j), the intersection point of the X-axis at 100 kHz refers to the series resistance (R_{series}). The first semicircle due to the SEI (R_{SEI}) can be identified between the frequency range of 100 kHz to 10 kHz, while the second semicircle of the charge transfer (R_{CT}) can be identified between the frequency range of 10 kHz to 10 Hz. The impedance response at lower frequencies between 10 Hz to 10 mHz seen as an angular line is generally attributed to diffusion processes [92]. Furthermore, the CPE_1 and CPE_2 reflect the double layer capacitance of the surface of SEI and active particles.

Figures 7(b)–(d) shows the Nyquist plots for full capacity cycling (3579 mAh g^{-1}) after 20, 50 and 100 cycles respectively, while figures 7(h)–(j) are the Nyquist plots for half capacity cycling (1800 mAh g^{-1}) at the same cycle numbers. It is clear that in both cycling conditions, the high frequency and medium-high frequency (100—10 kHz) responses of Formulation B increase the most significantly, being much larger than other formulations after 100 cycles. In accordance with cycling performance in 2 a and 2b, this indicates that the main failure mechanisms of the Si-dominant electrodes are caused by significant increases in both series resistance and SEI resistance.

With reference to figures 7(e)–(g) and (k)–(m), the fitted impedance data of longer term cycling at full and half capacity respectively, there is a clear alignment with features of the corresponding Nyquist plots in figures 7(b)–(d) and (h)–(j). Generally, the series resistance (R_{series}) gradually increases upon cycling (as shown in figures 7(e) and (k)), which can be caused by structural degradation within electrodes, during the volume changes as a function of cycle number. It can also be observed that for electrodes containing mainly Si (Formulation B) cycled at full capacity (figure 7(f)), there is significant growth in series resistance after 30 cycles. This is likely to be caused by severe electrode pulverisation, which consumes a large quantity of Li ions when forming new SEI. This is a continual process which reduces the Li-ion concentration in the electrolyte, thus decreasing the ionic conductivity. Similar behaviour has also been noticed for the Si-dominant electrode (Formulation B) cycled under half capacity (figure 7(k)).

As observed in figures 7(f) and (l), the R_{SEI} generally increases with the cycle number, which indicates that the SEI layer is continuously growing caused by electrode pulverisation under large volume changes. The Si only electrodes (Formulation B) exhibit a steep rise in the R_{SEI} after 50 cycles at full capacity cycles (figure 7(f)) due to the onset of severe electrode pulverisation, whereas the same situation is delayed up to 160 cycles for half capacity cycling (figure 7(l)). Comparing with that, Si-graphene electrodes and particularly the Si-FLG_{WJM} demonstrate much more stable R_{SEI} over cycling. It is possibly because the FLG_{WJM} flakes assist to maintain a stable structure under the large volume changes of SiNPs and postpone the significant electrode pulverisation, thereby, reduce the

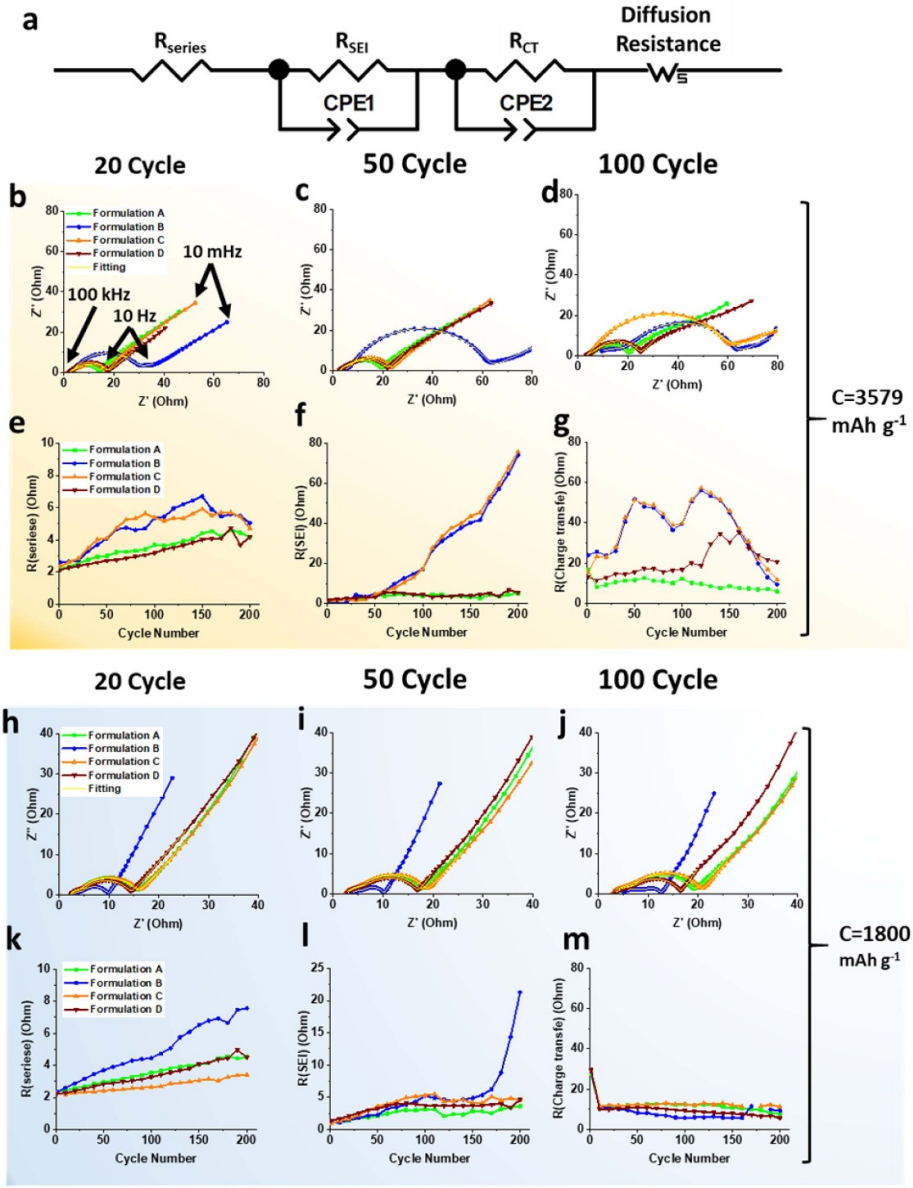

Figure 7. (a) The electrochemical equivalent circuit used for fitting the Nyquist plots; Nyquist plots during the charging process for all formulations cycled with full capacity of silicon (3579 mAh g^{-1}) after (b) 10 cycles, (c) 50 cycles and (d) 100 cycles and its fitting result for the full cycle range of (e) series resistance (f) SEI resistance (g) charge transfer resistance; with half capacity of silicon (1800 mAh g^{-1}) after (e) 10 cycles, (f) 50 cycles and (g) 100 cycles and the its impedance fitting results at full cycle range of (h) series resistance (i) SEI resistance (j) charge transfer resistance. The legends for (b) also applies to (c)–(m).

opportunity to form new SEI on the freshly exposed Si surface.

It can be observed from figure 7(m) that for all electrodes cycled under half capacity, the R_{CT} is mostly maintained at a relatively stable level.

The initial decrease for the first 10 cycles can be explained as a result of denser packing of active particles with conductive graphene networks, under internal pressure from Si's large volume expansion [92]. While cycled under full capacity (figure 7(g)), for electrodes with Formulation B, C & D, the R_{CT} increased after a few cycles and exponentially declines thereafter. To explain the R_{CT} result, it is better to firstly understand that the CT process normally involves two steps, namely, de-solvation of the solvated Li^+ ions in the electrolyte and transportation of these Li ions through the particle surface until it accepts an electron at the electrode's surface [44, 93]. Therefore, it is possible that when the internal pores being clogged up with SEI species [32, 61], there are less available Li ions to be de-solvated and transported to particle surface, which in turn increase the R_{CT}.

This situation will be changed when there are large cracks appearing within electrode. The large voids allow comparatively easy transportation of electrolytes within the electrode and thereby facilitate the availability of Li ions to be transferred onto the surface of active particles, thus reduced the R_{CT} [44].

However, for electrodes with Formulation A, it can be noticed that the R_{CT} remains at a stable level even cycled under the full capacity. It indicates that there is neither significant electrochemical agglomeration nor severe electrode pulverisation occurs during first 200 cycles. This is agreement with our tortuosity findings in figure 6, which also supports our hypothesis that the synergistic effect of Si and FLG in the electrode composite enhances the cycling longevity, as FLG_{WJM} flakes impart long-range charge transfer networks and mechanical rigidity. Additionally, any pulverized Si particles could precipitate onto FLG_{WJM} flake surfaces and thereby still be electrically connected to contribute to capacity.

3. Conclusions

This study demonstrates that a facile one-step wet-jet milling applied to a dispersion of silicon and graphite, leads to a Si-FLG_{WJM} composite that constitutes a high-performance anode. This exhibits enhanced capacity retention and the ability to function at a higher current density of 716 mA g^{-1}. In this composite, the SiNPs remain sandwiched between few-layer graphene flakes, the latter obtained by the direct liquid-phase exfoliation of graphite. Silicon and FLG_{WJM} form a layered porous conductive network. The uniform distribution of SiNPs on the FLG_{WJM} flakes surface forms an optimised ion-conducting channel structure, allowing the effective transport of electrons and Li-ions with unconstrained electrolyte movement. This Si-FLG_{WJM} composite powder when used as anodic material yields highly reversible electrochemical performance (reversible discharge capacity >1763 mAh g^{-1} after 450 cycles) with exceptional capacity retention and higher rate-capacity compared to the Si-dominant electrode or to electrodes obtained by simply mixing Si and FLG_{WJM} or commercial graphene nano-platelets. The superior stable cycling and rate performance of the Si-FLG_{WJM} composite electrode can be attributed to several factors:

(i) the high surface area of FLG_{WJM} flakes, with enhanced electrical conductivity (providing increased electron transport pathways between the silicon particles);
(ii) the highly porous network of Si-FLG_{WJM} composite allowing facile pathways for electrons and lithium ions, enhancing the electrical conductivity and lithium diffusion rate;
(iii) the voids surrounding the SiNPs can accommodate the volume changes from silicon particles (essential for superior performance);
(iv) the FLG_{WJM} flakes restricts the silicon particle from electrochemical fusion (coalescence) resulting in more stable electrochemical performance; and
(v) the planar FLG_{WJM} flakes-like structure imparts a degree of flexibility to the electrodes and thereby endure the volume strains during silicon lithiation.

Due to the 3D carbonaceous framework, the Si-FLG_{WJM} composite electrode demonstrates excellent cycling stability even under silicon's full capacity cycling. This excellent performance with further optimisation of the electrode formulation is propounded to improve high-capacity cycling stability and also scalability of the product makes it a prospectus anode material for LIBs.

4. Experimental

4.1. Synthesis of graphene powder (FLG_{WJM})

Graphene was prepared starting from natural graphite (+100 mesh, Sigma Aldrich) following the method developed by Del Rio-Castillo *et al* [43]. Graphite is dispersed in N-methyl-2-pyrrolidinone (NMP) solvent (>97%, Sigma Aldrich) in order to obtain a dispersion of 100 g of powder in 10 l of solvent. Then, the dispersion was subjected to a wet-jet milling procedure [43] to allow the exfoliation of graphite in few-layer graphene flakes. In this process, the exfoliation of graphite is promoted by the shearing forces due to the turbulent flow of the solvent forced to pass through the nozzles. Figure S11 reports representative Raman spectra for FLG_{WJM} and GNPs. The Raman analysis reveals the higher quality in terms of defects and number of layers of the FLG_{WJM} material.

4.2. Synthesis of silicon-graphene (Si-FLG_{WJM}) powder

Si-FLG_{WJM} composite powder was prepared following a modified wet-jet milling procedure. In this case, a mixture of graphite particles (+100 mesh, Sigma Aldrich) and silicon powder (<100 nm, Sigma Aldrich) in equal amount were dispersed in NMP solvent (>97%, Sigma Aldrich) in order to obtain a dispersion of 100 g of powder in 10 l of solvent. The dispersion was mechanically mixed on a stirrer to homogenize the dispersed flakes/powders. Following this, the mixture passed through a series of nozzles of wet-jet mill apparatus following the procedure details in Del Rio Castillo *et al* [43]. The wet-jet mill apparatus allows for the simultaneous exfoliation of graphite and the disaggregation of silicon particles, with their distribution onto the graphene flakes. This occurs by creating a turbulent flow when the solvent is forced to pass through the nozzles. By using the wet-jet milling technique, disaggregation of silicon particle is promoted by the collision of the particles in a highly pressurized stream of liquid dispersion. The simultaneous exfoliation of graphite is promoted by shearing forces, due to the turbulent flow of solvent forced

to pass through the nozzles. To obtain the final as-synthesized powder, the solvent was evaporated by a rota-vapour and the powder was dried overnight under dynamic vacuum at 70 °C.

4.3. Electrode materials

Four different formulations were generated to fabricate the electrode dispersions starting from Si-FLG_{WJM} composite powder, μm sized silicon powder with average particle size of 2.2 μm (Elkem Silgrain e-Si), nm Si powder with average particle size of <100 nm (Sigma Aldrich), as-synthesised graphene powder and commercial GNPs (thickness of 6–8 nm, XG Sciences). For the conductive additive, carbon black (Super C65, TIMCAL C-NERGY) was used. The aqueous-soluble binder used was partially neutralized polyacrylic acid (PAA), made from PAA powder (average Mw ~ 450 000, Sigma-Aldrich) and sodium hydroxide (according to the procedure proposed by Huang *et al* [31]). Figure 1(a) outlines all the formulation information for this study.

4.4. Electrodes preparation

For a typical Si-graphene composite anode, the initial electrode dispersion consisted of silicon graphene powder, conductive carbon black and water as the solvent (for every 10 g of silicon 20 g of deionised water was added). The components were dispersed in a high-speed Homodisperser (Model 2.5, PRIMIX) for 30 min at 1000 rpm. The resulting mixture was ultrasonically processed (UP400S, SciMED) for two periods at 60% amplitude for 7.5 min each. Following this, the Na-PAA binder was added to the dispersion prior to high-speed homodispersion for 30 min at 1000 rpm. Finally, the dispersion was transferred to a Filmix disperser (Model 40–40, PRIMIX, Japan) for homogenisation and breakdown of any secondary agglomeration. This was a two-step process, first at 10 ms^{-1} for 30 s and then at 25 ms^{-1} for 30 s. The coating process involved spreading the as-prepared dispersion onto a current collector of copper foil (10 μm, Oak Mitsui, electrodeposited) using a draw-down coater with a spreading blade (K control coater Model 101, RK Print, UK). The blade gap between the blade tip and the copper foil can be adjusted between the range 0–100 mm, for this study, a blade gap of 100 μm was used. Following deposition onto copper foil, the coating was dried on a preheated hot plate, set at a temperature of 50 °C. The coating was subsequently vacuum dried at 50 °C for an overnight period. Finally, electrodes were prepared from the coatings in a dry room (with a dew point of −45 °C) to ensure there was no exposure to moisture during the cell assembly process [44]. The mass loading of the dry film was 1.14 ± 0.18 mg cm^{-2} in the cut out electrode. More details on the specifications of each set of electrodes are presented in Table S3.

4.5. Electrochemical testing

For electrochemical tests, 2032 coin cells were assembled using Si-FLGWJM based electrodes as the working electrode and a lithium foil (diameter = 15.6 mm, PI-KEM) as counter electrode. The separator was PP/PE/PP microporous trilayer membrane (Celgard 2325) and the electrolyte used was RD265 (100 μl; 1.2 M LiPF6 in ethyl carbonate/ethyl methyl carbonate (1/3 v/v), 15% fluoroethylene carbonate and 3% vinylene carbonate) (PuriEL, SoulBrain). The spacer thickness was varied to achieve a uniform compression on all the electrodes by compressing the springs between 70%–80% [44].

Electrochemical performance was characterised using a multi-channel potentiostat, VMP3 (Bio-Logic) at room temperature. For the first cycle a C-rate of C/20 was used to initiate SEI formation and from the second cycle, a rate of C/5 was applied where C denotes capacity of the cell (1 C = 3579).

Further galvanostatic tests were carried out limiting the cell capacity at 1800 mAh g^{-1}, stopping the discharge/recharge at 2.5 h (50% state of charge) to minimise any pulverisation from large volume expansion upon lithiation [59] for improved cycle life.

Electrochemical Impedance spectra (EIS) were recorded at the end of the first cycle and repeated every 10 cycles.

4.6. Electrodes flexibility characterisation

The nano-indentation test was conducted using a Berkovich nano-indenter (NanoTest Extreme, Micro Materials Ltd, UK) and is reported in detail in our previous work Malik *et al* [44]. Figure S12 summarizes the results of these tests and highlights the effective better mechanical flexibility to accommodate volume expansion stresses induced by graphene.

4.7. SEM and FIB-SEM characterisation

After completion of cycling, the cell was disassembled in a glove box under an argon atmosphere. SEM characterisation was performed with field-emission SEM microscope (Sigma, Carl Zeiss, Germany). Cycled electrodes were then transferred to the focused ion beam in conjunction with scanning electron microscopy (FIB-SEM, Scios, FEI) instrument for cross-sectional analysis and tomography, to understand the microstructural evolution of the Si-graphene electrodes. From the cross-sectional images, the thickness of electrodes excluding the copper foil was measured. The 3D tomography dataset were collected automatically using 'slice and view' software (FEI) and is reported in detail in our previous work Malik *et al* [44] (see also figure S13 and related discussion).

4.8. Image processing

The detailed image processing steps of SEM images from FIB-SEM is reported in our previous work Malik *et al* [44].

Acknowledgments

This project has received funding from the European Union's Horizon 2020 research and innovation program under the grant agreement No. 696656—GrapheneCore2 and the grant agreement No. 881603—GrapheneCore3. The authors also acknowledge the ISCF Faraday Challenge project "Towards a Comprehensive Understanding of Degradation Processes in EV Batteries" for funding under EP/S003053/1.

ORCID iDs

Romeo Malik
https://orcid.org/0000-0003-0206-7084
Laura Silvestri
https://orcid.org/0000-0002-5649-8237
Francesco Bonaccorso
https://orcid.org/0000-0001-7238-9420
Melanie J Loveridge
https://orcid.org/0000-0003-2908-3885

References

[1] Liu N, Wu H, McDowell M T, Yao Y, Wang C and Cui Y 2012 A yolk-shell design for stabilized and scalable Li-ion battery alloy anodes *Nano Lett.* **12** 3315–21
[2] Li J and Dahn J R 2007 An in situ x-ray diffraction study of the reaction of Li with crystalline Si *J. Electrochem. Soc.* **154** A156
[3] Obrovac M N and Chevrier V L 2014 Alloy Negative Electrodes for Li-Ion Batteries *Chem. Rev.* **114** 11444–502
[4] Obrovac M N and Krause L J 2007 Reversible cycling of crystalline silicon powder *J. Electrochem. Soc.* **154** A103
[5] Qiao L, Sun X, Yang Z, Wang X, Wang Q and He D 2013 Network structures of fullerene-like carbon core/nano-crystalline silicon shell nanofibers as anode material for lithium-ion batteries *Carbon N. Y.* **54** 29–35
[6] Kim S *et al* 2014 High-yield synthesis of single-crystal silicon nanoparticles as anode materials of lithium ion batteries via photo sensitizer-assisted laser pyrolysis *J. Mater. Chem.* A **2** 18070–5
[7] Ko M, Chae S and Cho J 2015 Challenges in accommodating volume change of Si anodes for Li-ion batteries *ChemElectroChem* **2** 1645–51
[8] Li X, Gu M, Hu S, Kennard R, Yan P, Chen X, Wang C, Sailor M J, Zhang J G and Liu J 2014 Mesoporous silicon sponge as an anti-pulverization structure for high-performance lithium-ion battery anodes *Nat. Commun.* **5** 4105
[9] McDowell M T, Lee S W, Nix W D and Cui Y 2013 25th anniversary article: understanding the lithiation of silicon and other alloying anodes for lithium-ion batteries *Adv. Mater.* **25** 4966–85
[10] Kulova T L, Skundin A M, Pleskov Y V, Terukov E I and Kon'kov O I 2007 Lithium insertion into amorphous silicon thin-film electrodes *J. Electroanal. Chem.* **600** 217–25
[11] Chevrier V L, Liu L, Le D B, Lund J, Molla B, Reimer K, Krause L J, Jensen L D, Figgemeier E and Eberman K W 2014 Evaluating Si-based materials for Li-ion batteries in commercially relevant negative electrodes *J. Electrochem. Soc.* **161** A783–91
[12] Kasavajjula U, Wang C and Appleby A J 2007 Nano- and bulk-silicon-based insertion anodes for lithium-ion secondary cells *J. Power Sources* **163** 1003–39
[13] Kim H, Seo M, Park M-H and Cho J 2010 A critical size of silicon nano-anodes for lithium rechargeable batteries *Angew. Chem. Int. Ed.* **49** 2146–9
[14] Wu H and Cui Y 2012 Designing nanostructured Si anodes for high energy lithium ion batteries *Nano Today* **7** 414–29
[15] Zhang W-J 2011 A review of the electrochemical performance of alloy anodes for lithium-ion batteries *J. Power Sources* **196** 13–24
[16] Zhang Q, Yu Z, Du P and Su C 2010 Carbon nanomaterials used as conductive additives in lithium ion batteries *Recent Pat. Nanotechnol.* **4** 100–10
[17] Bridel J S, Azaïs T, Morcrette M, Tarascon J M and Larcher D 2010 Key parameters governing the reversibility of Si/carbon/CMC electrodes for Li-ion batteries *Chem. Mater.* **22** 1229–41
[18] Guo J and Wang C 2010 A polymer scaffold binder structure for high capacity silicon anode of lithium-ion battery *Chem. Commun.* **46** 1428–30
[19] Hu Y S, Demir-Cakan R, Titirici M M, Müller J O, Schlögl R, Antonietti M and Maier J 2008 Superior storage performance of a Si@SiO_x/C nanocomposite as anode material for lithium-ion batteries *Angew. Chem. Int. Ed.* **47** 1645–9
[20] Bordes A, Eom K and Fuller T F 2014 The effect of fluoroethylene carbonate additive content on the formation of the solid-electrolyte interphase and capacity fade of Li-ion full-cell employing nano Si-graphene composite anodes *J. Power Sources* **257** 163–9
[21] Bai X, Yu Y, Kung H H, Wang B and Jiang J 2016 Si@SiO_x/graphene hydrogel composite anode for lithium-ion battery *J. Power Sources* **306** 42–48
[22] Chabot V, Feng K, Park H W, Hassan F M, Elsayed A R, Yu A, Xiao X and Chen Z 2014 Graphene wrapped silicon nanocomposites for enhanced electrochemical performance in lithium ion batteries *Electrochim. Acta* **130** 127–34
[23] Xin X, Zhou X, Wang F, Yao X, Xu X, Zhu Y and Liu Z 2012 A 3D porous architecture of Si/graphene nanocomposite as high-performance anode materials for Li-ion batteries *J. Mater. Chem.* **22** 7724–30
[24] Zhao X, Hayner C M, Kung M C and Kung H H 2011 In-plane vacancy-enabled high-power Si-graphene composite electrode for lithium-ion batteries *Adv. Energy Mater.* **1** 1079–84
[25] Novoselov K S, Geim A K, Morozov S V, Jiang D, Zhang Y, Dubonos S V, Grigorieva I V and Firsov A A 2004 Electric field effect in atomically thin carbon films *Science* **306** 666–9
[26] Geim A K and Novoselov K S 2007 The rise of graphene *Nat. Mater.* **6** 183–91
[27] Greco E, Nava G, Fathi R, Fumagalli F, Del Rio-Castillo A E, Ansaldo A, Monaco S, Bonaccorso F, Pellegrini V and Di Fonzo F 2017 Few-layer graphene improves silicon performance in li-ion battery anodes *J. Mater. Chem.* A **5** 19306–15
[28] Palumbo S, Silvestri L, Ansaldo A, Brescia R, Bonaccorso F and Pellegrini V 2019 Silicon few-layer graphene nanocomposite as high-capacity and high-rate anode in lithium-ion batteries *ACS Appl. Energy Mater.* **2** 1793–802
[29] Tao Y *et al* 2013 Towards ultrahigh volumetric capacitance: graphene derived highly dense but porous carbons for supercapacitors *Sci. Rep.* **3** 1–8
[30] Loveridge M J, Lain M J, Huang Q, Wan C, Roberts A J, Pappas G S and Bhagat R 2016 Enhancing cycling durability of Li-ion batteries with hierarchical structured silicon-graphene hybrid anodes *Phys. Chem. Chem. Phys.* **18** 30677–85
[31] Huang Q, Loveridge M J, Genieser R, Lain M J and Bhagat R 2018 Electrochemical evaluation and phase-related

impedance studies on silicon-few layer graphene (FLG) composite electrode systems *Sci. Rep.* **8** 1386
[32] Radvanyi E, Porcher W, De Vito E, Montani A, Franger S, Jouanneau S and Larbi S 2014 Failure mechanisms of nano-silicon anodes upon cycling: an electrode porosity evolution model *Phys. Chem. Chem. Phys.* **16** 17142–53
[33] Wong D P, Tseng H P, Chen Y T, Hwang B J, Chen L C and Chen K H 2013 A stable silicon/graphene composite using solvent exchange method as anode material for lithium ion batteries *Carbon N. Y.* **63** 397–403
[34] Cui L-F, Hu L, Wook J and Cui Y 2010 Light-weight free-standing carbon nanotube-silicon films for anodes of lithium ion batteries *ACS Nano* **4** 3671–8
[35] Ren J G, Wu Q H, Hong G, Zhang W J, Wu H, Amine K, Yang J and Lee S T 2013 Silicon-graphene composite anodes for high-energy lithium batteries *Energy Technol.* **1** 77–84
[36] Xiao Q, Zhang Q, Fan Y, Wang X and Susantyoko R A 2014 Soft silicon anodes for lithium ion batteries *Energy Environ. Sci.* **7** 2261
[37] Zhang B, Zheng Q B, Huang Z D, Oh S W and Kim J K 2011 SnO_2-graphene-carbon nanotube mixture for anode material with improved rate capacities *Carbon* **49** 4524–34
[38] Wang B, Li X, Zhang X, Luo B, Jin M, Liang M, Dayeh S A, Picraux S T and Zhi L 2013 Adaptable silicon-carbon nanocables sandwiched between reduced graphene oxide sheets as lithium ion battery anodes *ACS Nano* **7** 1437–45
[39] Wang J Z, Zhong C, Chou S L and Liu H K 2010 Flexible free-standing graphene-silicon composite film for lithium-ion batteries *Electrochem. Commun.* **12** 1467–70
[40] Chang J, Huang X, Zhou G, Cui S, Hallac P B, Jiang J, Hurley P T and Chen J 2014 Multilayered Si nanoparticle/reduced graphene oxide hybrid as a high-performance lithium-ion battery anode *Adv. Mater.* **26** 758–64
[41] Liang G, Qin X, Zou J, Luo L, Wang Y, Wu M, Zhu H, Chen G, Kang F and Li B 2018 Electrosprayed silicon-embedded porous carbon microspheres as lithium-ion battery anodes with exceptional rate capacities *Carbon* **127** 424–31
[42] Wu J, Qin X, Zhang H, He Y B, Li B, Ke L, Lv W, Du H, Yang Q H and Kang F 2015 Multilayered silicon embedded porous carbon/graphene hybrid film as a high performance anode *Carbon* **84** 434–43
[43] Del Rio Castillo A E *et al* 2018 High-yield production of 2D crystals by wet-jet milling *Mater. Horiz.* **5** 890–904
[44] Malik R, Loveridge M J, Williams L J, Huang Q, West G, Shearing P R, Bhagat R and Walton R I 2019 Porous metal-organic frameworks for enhanced performance silicon anodes in lithium-ion batteries *Chem. Mater.* **31** 4156–65
[45] An W, Gao B, Mei S, Xiang B, Fu J, Wang L, Zhang Q, Chu P K and Huo K 2019 Scalable synthesis of ant-nest-like bulk porous silicon for high-performance lithium-ion battery anodes *Nat. Commun.* **10** 1447
[46] Magasinski A, Dixon P, Hertzberg B, Kvit A, Ayala J and Yushin G 2010 High-Performance Lithium-Ion Anodes Using a Hierarchical Bottom-up Approach *Nat. Mater.* **9** 353–8
[47] Li B, Yao F, Bae J J, Chang J, Zamfir M R, Le D T, Pham D T, Yue H and Lee Y H 2015 Hollow carbon nanospheres/silicon/alumina core-shell film as an anode for lithium-ion batteries *Sci. Rep.* **5** 7659
[48] Chen X, Li X, Ding F, Xu W, Xiao J, Cao Y, Meduri P, Liu J, Graff G L and Zhang J G 2012 Conductive rigid skeleton supported silicon as high-performance Li-ion battery anodes *Nano Lett.* **12** 4124–30
[49] Ko M, Chae S, Ma J, Kim N, Lee H W, Cui Y and Cho J 2016 Scalable synthesis of silicon-nanolayer-embedded graphite for high-energy lithium-ion batteries *Nat. Energy* **1** 16113
[50] Kim S Y, Lee J, Kim B H, Kim Y J, Yang K S and Park M S 2016 Facile synthesis of carbon-coated silicon/graphite spherical composites for high-performance lithium-ion batteries *ACS Appl. Mater. Interfaces* **8** 12109–17
[51] Chae C, Noh H J, Lee J K, Scrosati B and Sun Y K 2014 A high-energy li-ion battery using a silicon-based anode and a nano-structured layered composite cathode *Adv. Funct. Mater.* **24** 3036–42
[52] Xu Q, Li J-Y, Sun J-K, Yin Y-X, Wan L-J and Guo Y-G 2017 Watermelon-inspired Si/C microspheres with hierarchical buffer structures for densely compacted lithium-ion battery anodes *Adv. Energy Mater.* **7** 1601481
[53] Zhou W, Upreti S and Whittingham M S 2011 High performance Si/MgO/graphite composite as the anode for lithium-ion batteries *Electrochem. Commun.* **13** 1102–4
[54] Tao H C, Fan L Z, Mei Y and Qu X 2011 Self-supporting Si/reduced graphene oxide nanocomposite films as anode for lithium ion batteries *Electrochem. Commun.* **13** 1332–5
[55] Park S H, Kim H K, Ahn D J, Lee S I, Roh K C and Kim K B 2013 Self-assembly of Si entrapped graphene architecture for high-performance Li-ion batteries *Electrochem. Commun.* **34** 117–20
[56] Lee J K, Smith K B, Hayner C M and Kung H H 2010 Silicon nanoparticles-graphene paper composites for Li ion battery anodes *Chem. Commun.* **46** 2025–7
[57] Mori T, Chen C J, Hung T F, Mohamed S G, Lin Y Q, Lin H Z, Sung J C, Hu S F and Liu R S 2015 High specific capacity retention of graphene/silicon nanosized sandwich structure fabricated by continuous electron beam evaporation as anode for lithium-ion batteries *Electrochim. Acta* **165** 166–72
[58] Tang H, Zhang Y J, Xiong Q Q, Cheng J D, Zhang Q, Wang X L, Gu C D and Tu J P 2015 Self-assembly silicon/porous reduced graphene oxide composite film as a binder-free and flexible anode for lithium-ion batteries *Electrochim. Acta* **156** 86–93
[59] Obrovac M N and Christensen L 2004 Structural changes in silicon anodes during lithium insertion/extraction *Electrochem. Solid-State Lett.* **7** A93
[60] Shi F, Song Z, Ross P N, Somorjai G A, Ritchie R O and Komvopoulos K 2016 Failure mechanisms of single-crystal silicon electrodes in lithium-ion batteries *Nat. Commun.* **7** 1–8
[61] Vetter J, Novak P, Wagner M R, Veit C, Moller K C, Besenhard J O, Winter M, Wohlfahrt-Mehrens M, Vogler C and Hammouche A 2005 Ageing mechanisms in lithium-ion batteries *J. Power Sources* **147** 269–81
[62] Zou J, Sole C, Drewett N E and Hardwick L J 2016 In situ study of Li intercalation into highly crystalline graphitic flakes of varying thicknesses *J. Phys. Chem. Lett.* **7** 4291–6
[63] Cui L, Yang Y, Hsu C and Cui Y 2009 Carbon - silicon core - shell nanowires as high capacity electrode for lithium ion batteries 2009 *Nano Lett.* **9** 3370–4
[64] Datta M K and Kumta P N 2009 In situ electrochemical synthesis of lithiated silicon-carbon based composites anode materials for lithium ion batteries *J. Power Sources* **194** 1043–52
[65] Ohzuku T 1993 Formation of lithium-graphite intercalation compounds in nonaqueous electrolytes and their application as a negative electrode for a lithium ion (Shuttlecock) cell *J. Electrochem. Soc.* **140** 2490
[66] Shim J and Striebel K A 2004 The dependence of natural graphite anode performance on electrode density *J. Power Sources* **130** 247–53
[67] Ogata K, Salager E, Kerr C J, Fraser A E, Ducati C, Morris A J, Hofmann S and Grey C P 2014 revealing lithium–silicide phase transformations in nano-structured silicon-based lithium ion batteries via in situ NMR spectroscopy *Nat. Commun.* **5** 3217
[68] Güneş F 2016 A direct synthesis of Si-nanowires on 3D porous graphene as a high performance anode material for li-ion batteries *RSC Adv.* **6** 1678–85
[69] Li Z F, Zhang H, Liu Q, Liu Y, Stanciu L and Xie J 2014 Novel pyrolyzed polyaniline-grafted silicon nanoparticles encapsulated in graphene sheets as li-ion battery anodes *ACS Appl. Mater. Interfaces* **6** 5996–6002

[70] Ji J, Ji H, Zhang L L, Zhao X, Bai X, Fan X, Zhang F and Ruoff R S 2013 Graphene-encapsulated Si on ultrathin-graphite foam as anode for high capacity lithium-ion batteries *Adv. Mater.* **25** 4673–7
[71] Kang I, Jang J, Kim M S, Park J W, Kim J H and Cho Y W 2017 Nanostructured silicon/silicide/carbon composite anodes with controllable voids for Li-ion batteries *Mater. Des.* **120** 230–7
[72] Biton M, Yufit V, Tariq F, Kishimoto M and Brandon N 2017 Enhanced imaging of lithium ion battery electrode materials *J. Electrochem. Soc.* **164** 6032–8
[73] Liu H, Foster J M, Gully A, Krachkovskiy S, Jiang M, Wu Y, Yang X, Protas B, Goward G R and Botton G A 2016 Three-dimensional investigation of cycling-induced microstructural changes in lithium-ion battery cathodes using focused ion beam/scanning electron microscopy *J. Power Sources* **306** 300–8
[74] Etiemble A, Tranchot A, Douillard T, Idrissi H, Maire E and Roue L 2016 Evolution of the 3D microstructure of a si-based electrode for Li-ion batteries investigated by FIB/SEM tomography *J. Electrochem. Soc.* **163** 1550–9
[75] Zielke L, Hutzenlaub T, Wheeler D R, Manke I, Arlt T, Paust N, Zengerle R and Thiele S 2014 A combination of x-ray tomography and carbon binder modeling: reconstructing the three phases of $LiCoO_2$ Li-ion battery cathodes *Adv. Energy Mater.* **4** 1301617
[76] Zielke L, Hutzenlaub T, Wheeler D R, Chao C-W, Manke I, Hilger A, Paust N, Zengerle R and Thiele S 2015 Three-phase multiscale modeling of a $LiCoO_2$ cathode: combining the advantages of FIB–SEM imaging and x-ray tomography *Adv. Energy Mater.* **5** 1401612
[77] Ender M, Joos J, Carraro T and Ivers-Tiffee E 2012 Quantitative characterization of $LiFePO_4$ cathodes reconstructed by FIB/SEM tomography *J. Electrochem. Soc.* **159** A972–80
[78] Chen-Wiegart Y K, DeMike R, Erdonmez C, Thornton K, Barnett S A and Wang J 2014 Tortuosity characterization of 3d microstructure at nano-scale for energy storage and conversion materials *J. Power Sources* **249** 349–56
[79] Liu Z, Scott Cronin J, Chen-Wiegart Y C K, Wilson J R, Yakal-Kremski K J, Wang J, Faber K T and Barnett S A 2013 Three-dimensional morphological measurements of $LiCoO_2$ and $LiCoO_2/Li(Ni_{1/3}Mn_{1/3}Co_{1/3})O_2$ lithium-ion battery cathodes *J. Power Sources* **227** 267–74
[80] Stephenson D E, Walker B C, Skelton C B, Gorzkowski E P, Rowenhorst D J and Wheeler D R 2011 Modeling 3D microstructure and ion transport in porous Li-ion battery electrodes *J. Electrochem. Soc.* **158** A781–9
[81] Gully A, Liu H, Srinivasan S, Sethurajan A K, Schougaard S and Protas B 2014 Effective transport properties of porous electrochemical materials — a homogenization approach *J. Electrochem. Soc.* **161** E3066–77
[82] Ender M, Joos J, Carraro T and Ivers-Tiffée E 2011 Three-dimensional reconstruction of a composite cathode for lithium-ion cells *Electrochem. Commun.* **13** 166–8
[83] Wilson J R, Cronin J S, Barnett S A and Harris S J 2011 Measurement of three-dimensional microstructure in a $LiCoO_2$ positive electrode *J. Power Sources* **196** 3443–7
[84] Garcĩa R E and Chiang Y M 2007 Spatially resolved modeling of microstructurally complex battery architectures *J. Electrochem. Soc.* **154** A856
[85] Vierrath S, Zielke L, Moroni R, Mondon A, Wheeler D R, Zengerle R and Thiele S 2015 Morphology of nanoporous carbon-binder domains in li-ion batteries - a FIB-SEM study *Electrochem. Commun.* **60** 176–9
[86] Wilson J R, Kobsiriphat W, Mendoza R, Chen H-Y, Hiller J M, Miller D J, Thornton K, Voorhees P W, Adler S B and Barnett S A 2006 Three-dimensional reconstruction of a solid-oxide fuel-cell anode *Nat. Mater.* **5** 541–4
[87] Karki K, Epstein E, Cho J H, Jia Z, Li T, Picraux S T, Wang C and Cumings J 2012 Lithium-assisted electrochemical welding in silicon nanowire battery electrodes *Nano Lett.* **12** 1392–7
[88] Philippe B, Dedryveère R, Gorgoi M, Rensmo H, Gonbeau D and Edström K 2013 Role of the $LiPF_6$ salt for the long-term stability of silicon electrodes in Li-ion batteries - a photoelectron spectroscopy study *Chem. Mater.* **25** 394–404
[89] Radvanyi E, De Vito E, Porcher W, Jouanneau S and Larbi S 2014 An XPS/AES comparative study of the surface behaviour of nano-silicon anodes for Li-ion batteries *J. Anal. At. Spectrom.* **29** 1120–31
[90] Etiemble A, Besnard N, Bonnin A, Adrien J, Douillard T, Tran-Van P, Gautier L, Badot J-C, Maire E and Lestriez B 2016 Multiscale morphological characterization of process induced heterogeneities in blended positive electrodes for lithium–ion batteries *J. Mater. Sci.* **52** 3576
[91] Kehrwald D, Shearing P R, Brandon N P, Sinha P K and Harris S J 2011 Local tortuosity inhomogeneities in a lithium battery composite electrode *J. Electrochem. Soc.* **158** A1393
[92] Guo J, Sun A, Chen X, Wang C and Manivannan A 2011 Cyclability study of silicon-carbon composite anodes for lithium-ion batteries using electrochemical impedance spectroscopy *Electrochim. Acta* **56** 3981–7
[93] Jow T R, Delp S A, Allen J L, Jones J-P and Smart M C 2018 Factors limiting Li^+ charge transfer kinetics in Li-ion batteries *J. Electrochem. Soc.* **165** A361–7